An Enhanced Geostationary Satellite–Based Convective Initiation Algorithm for 0–2-h Nowcasting with Object Tracking

JOHN R. WALKER

Earth System Science Center, University of Alabama in Huntsville, Huntsville, Alabama

WAYNE M. MACKENZIE JR.

Earth System Science Center, University of Alabama in Huntsville, Huntsville, Alabama, and Earth Resources Technology, Inc., Laurel, Maryland

JOHN R. MECIKALSKI

Department of Atmospheric Science, University of Alabama in Huntsville, Huntsville, Alabama

CHRISTOPHER P. JEWETT

Earth System Science Center, University of Alabama in Huntsville, Huntsville, Alabama

(Manuscript received 29 November 2011, in final form 20 June 2012)

ABSTRACT

This paper describes an enhanced 0–2-h convective initiation (CI) nowcasting algorithm known as Satellite Convection Analysis and Tracking, version 2 (SATCASTv2). Tracking of developing cumulus cloud ''objects'' in advance of CI was developed as a means of reducing errors caused by tracking single satellite pixels of cumulus clouds, as identified in Geostationary Operational Environmental Satellite (GOES) output. The method rests on the idea that cloud objects at one time, when extrapolated forward in space and time using mesoscale atmospheric motion vectors, will overlap with the same actual cloud objects at a later time. Significant overlapping confirms that a coherent cumulus cloud is present and trackable in GOES data and that it is persistent enough that various infrared threshold–based tests may be performed to assess cloud growth. Validation of the new object-tracking approach to nowcasting CI was performed over four regions in the United States: 1) Melbourne, Florida; 2) Memphis, Tennessee; 3) the central United States/Great Plains; and 4) the northeastern United States as a means of evaluating algorithm performance in various convective environments. In this study, 9943 CI nowcasts and 804 CI events were analyzed. Optimal results occurred in the central U.S./Great Plains domain, where the probability of detection (POD) and false-alarm ratio (FAR) reached 85% and 55%, respectively, for tracked cloud objects. The FARs were partially attributed to difficulties inherent to the CI nowcasting problem. PODs were seen to decrease for CI events in Florida. Discussion is provided on how SATCASTv2 performed, as well as on how certain problems may be mitigated, especially in light of enhanced geostationary-satellite systems.

1. Introduction

Convective initiation (CI) is a significant forecasting problem within the meteorological community. The inability to accurately forecast CI results in substantial costs to society through aviation and other industries that are affected by weather and through safety problems at large-scale social events. Given this significance, the research community has attempted to increase the understanding of the CI process, along with additional attempts to forecast its occurrence with substantial skill. There are several studies that investigate the physical processes of CI (Wilson et al. 1988; Wakimoto and Lew 1993; Weckwerth and Parson 2006); the focus of the paper presented here is the short-term forecasting (0–2 h) of CI using data from geostationary satellites—a process that is often referred to as ''nowcasting.'' For this study,

Corresponding author address: John R. Walker, University of Alabama in Huntsville, Earth System Science Center, 320 Sparkman Dr., Cramer Hall/#3075, Huntsville, AL 35805.
E-mail: jwalker@nsstc.uah.edu

DOI: 10.1175/JAMC-D-11-0246.1

CI is defined as the first occurrence of a radar echo of intensity ≥35 dBZ from a growing cumulus cloud, which follows similarly from several past studies (Browning and Atlas 1965; Marshall and Radhakant 1978; Wilson and Schreiber 1986; Wilson et al. 1992; Wilson and Mueller 1993; Mueller et al. 2003).

There are several tools available to aid in the nowcasting of CI. The analysis of surface observations to detect surface-based boundaries that are responsible for causing lift toward initiating convective storms is one of the most widely used techniques to identify regions where convective activity will likely develop (Banacos and Schultz 2005). These observations depict the current state of the near-surface atmosphere very well, but they are generally limited in spatial extent. The development of surface-station mesonetworks has mitigated some of these shortfalls, but these networks are limited to only a few local regions and do not provide enough detailed information about the environment above the surface.

The use of high-resolution numerical weather prediction (NWP) models has shown promise in identifying regions where CI may occur, especially as grid spacing decreases (Trentmann et al. 2009). Important details from these CI forecasts are often missing or incorrect, however, as a result of limitations from poor spatial resolution of input and output data and of the difficulties associated with data assimilation. Furthermore, because of current computer resource constraints, the high-resolution, cloud-resolving-scale NWP simulations needed to more accurately forecast CI can only be applied over small regional domains, making them intractable for general use by forecasters.

The use of radar data has proven to be extremely useful in CI nowcasting and in monitoring ongoing convection for severity. Radar has been used to identify surface boundaries and associated areas of upward vertical motion, making use of biological fliers (Bachmann and Zrnić 2007) and the refraction index from steep gradients of water vapor (Roberts et al. 2008). Outside of near-surface boundary detection, one disadvantage of using radar systems for the purpose of nowcasting CI is that relatively large objects (raindrops, insects, etc.) must be present in order for the radar beam to be reflected back to the receiver. As a result, although radar can certainly help to monitor areas of existing convective growth, most operational radar networks are currently not set up to adequately monitor vertical cloud growth prior to the development of significantly sizable hydrometeors. The ability to monitor such growth ahead of time would considerably enhance lead times for nowcasting CI. Furthermore, the spatial coverage of radar data is limited, especially over the oceans and in many land areas outside of the United States. This is, perhaps, the most limiting disadvantage of relying upon radar to help to forecast CI on a global scale.

Although some of the methods listed above are beneficial for determining which general regions are favorable for CI, they cannot accurately pinpoint specific areas where convection may develop. Determining the exact future locations of thunderstorms continues to be problematic and is of particular interest to the aviation community (Murray 2002; Mecikalski and Bedka 2006; Mecikalski et al. 2008)—a fact that motivates this study. This paper presents an updated method to identify, track, and monitor convective-type clouds down to scales near 4 km to determine the likelihood of mature convective storm development in the near future, that is, to nowcast CI. The updated method is deemed significantly better than either per-pixel cloud-tracking approaches or methods that do not identify cumulus clouds as unique, trackable features in satellite imagery. Section 2 provides an overview of previous studies that detail the use satellite data to monitor cloud growth. Section 3 provides the method for the new satellite-based CI nowcasting system. Section 4 covers results from the validation of the new system. Section 5 discusses some of the potential sources of error in this new system. Section 6 presents the main conclusions.

2. Background

Roberts and Rutledge (2003) examined several cases of convective storms that were triggered over eastern Colorado. They compared radar trends with satellite trends of the storms, specifically using the *Geostationary Operational Environmental Satellite* (*GOES*)*-8* visible and 10.8-μm infrared (IR) channels. The results demonstrated that, by monitoring the cloud-top properties for subfreezing temperatures and for significant thermal IR cooling rates, CI forecast lead times of ≥30 min can be provided before the first 35-dBZ radar reflectivity echo is detected. That study provided a framework for the development of a satellite-only CI forecasting system that could provide near-term CI nowcasts in radar-void areas; this algorithm was named the Satellite Convection Analysis and Tracking (SATCAST) system [based on Mecikalski and Bedka (2006)].

The original SATCAST had three main components. The first component identified only cumulus clouds, at various stages of growth, forming a convective cloud mask (CCM; Berendes et al. 2008). Next, a tracking method that used satellite-derived mesoscale atmospheric motion vectors (MAMVs; Velden et al. 1997, 1998; Bedka and Mecikalski 2005; Bedka et al. 2009) was employed to track individual cloud-top pixels between subsequent satellite images. Last, a multispectral approach for

monitoring the height and growth of cloud tops was used to determine which cloud pixels were most likely to be associated with future instances of CI. This multispectral approach incorporated the findings from Roberts and Rutledge (2003), along with information detailed in many other studies focusing on the utility of channel differencing and trending toward retrieving pertinent cloud-top-property information relevant to forecasting CI in the near future (Prata 1989; Ackerman et al. 1992; Ackerman 1996; Mecikalski and Bedka 2006; Mecikalski et al. 2008, 2010; also Strabala et al. 1994; Schmetz et al. 1997; Baum et al. 2000). This subsequently led to the development of threshold-based ''interest fields'' composed of a series of spectral and temporal differencing tests used to identify cumulus clouds that were more likely to develop into mature cumulonimbus in the 30–60-min time frame.

One of the main disadvantages of this original version of SATCAST was that the tracking was based on a single GOES pixel, leading to inaccuracies because it allowed for almost no margin of error in the MAMV-based tracking method. If a 1-km^2 cloud-top pixel was not tracked with high accuracy between two consecutive satellite-image scans (within the confines of a single 4-km^2 IR pixel), then the temporal trending interest fields would be incorrect. Inaccurate nowcasts of CI often resulted. In a later study, Mecikalski et al. (2008) quantitatively explored the effectiveness of the original SATCAST system by comparing the pixel-based output with radar data. While highlighting some of the disadvantages of the single-pixel algorithm, this study was also able to show the skill of the satellite-based CI nowcasting method. Mecikalski et al. (2010) subsequently emphasized the benefit of using a combination of satellite channels when monitoring vertical cloud growth. Despite these positive findings, one of the biggest issues to contend with in such a CI nowcasting system is the method used to track preconvective clouds between subsequent satellite images.

Sieglaff et al. (2011) introduced a CI system that monitored the temporal trend of cloud properties along with brightness temperatures T_B from the *GOES-12* 10.7-μm channel. That study provides an alternative to tracking cloud elements, incorporating a ''box average'' approach that centers a box of variable size over each IR satellite-image pixel and averages the brightness temperatures from all clouded pixels within the box. The purpose of the box-averaging approach is to more easily compute cloud-top cooling rates between two successive images at each pixel without the higher computational requirements associated with explicitly tracking cloud pixels. The theory behind this method is that cloud motion is inherently accounted for, assuming that a large enough set of box sizes will contain the cloud features of interest between consecutive satellite-image scans. This technique further assumes that, although the T_Bs of the convective clouds are averaged over a large area, the signal from any growing clouds remains. Two boxes are used for this, one with dimensions of 7 $\times$ 7 pixels, and the other with dimensions of 13 $\times$ 13 pixels, covering ~784 and ~2704 km^2, respectively, when using 4-km-spatial-resolution IR GOES data. The smaller box is used for the averaging of T_Bs, and the larger box is employed to help to mitigate errors and to limit false cooling signals. While this method is intuitive, it often does not allow for small-scale clouds (4–8 km^2) to be monitored and, therefore, cannot provide accurate CI forecasts for clouds possessing lower magnitudes of cloud-top cooling rates, because the weaker cooling signals tend to be diluted when performing spatial averaging within the box. To demonstrate how a local-area box-average approach can reduce the satellite retrieved signals of growing convective clouds, a case is presented in Fig. 1 over southwestern Mississippi for 7 June 2011 that compares the object-tracking method described within this paper with a box-averaging technique. In this case, the object-tracking method yields a 10.7-μm cloud-top cooling rate of -6.0 K (15 min)$^{-1}$ for a growing convective cloud, whereas the local-area average of cloud-pixel T_Bs contained within the given box—with dimensions of 28 km $\times$ 28 km, covering ~784 km^2—yields a cloud-top cooling rate of only -0.4 K (15 min)$^{-1}$. The cloud developed to the point of CI approximately 29 min after the 1902 UTC satellite scan. It is important to note that this demonstration does not represent an exact replication of the Sieglaff et al. (2011) box-average method and that the purpose here is simply to show that an object-based approach is better suited for monitoring smaller convective clouds, as compared with a general box-averaging approach.

In an effort to improve upon both of these methods, the technique developed in this study treats each convective cloud as a single entity when tracking and monitoring its growth, as opposed to employing either a single-pixel tracking approach or a broad-area box-averaging approach. This study will present an improved tracking method within the SATCAST algorithm, designed to track and monitor the growth of convective clouds at scales down to the spatial resolution provided by a given geostationary-satellite instrument (4 km on *GOES-12–15*; 3 km on Meteosat Second Generation; 2 km on the forthcoming GOES-R). This new algorithm is referred to as ''SATCASTv2.''

3. Method

The SATCASTv2 algorithm is broken into six main components: 1) satellite data download, 2) MAMV

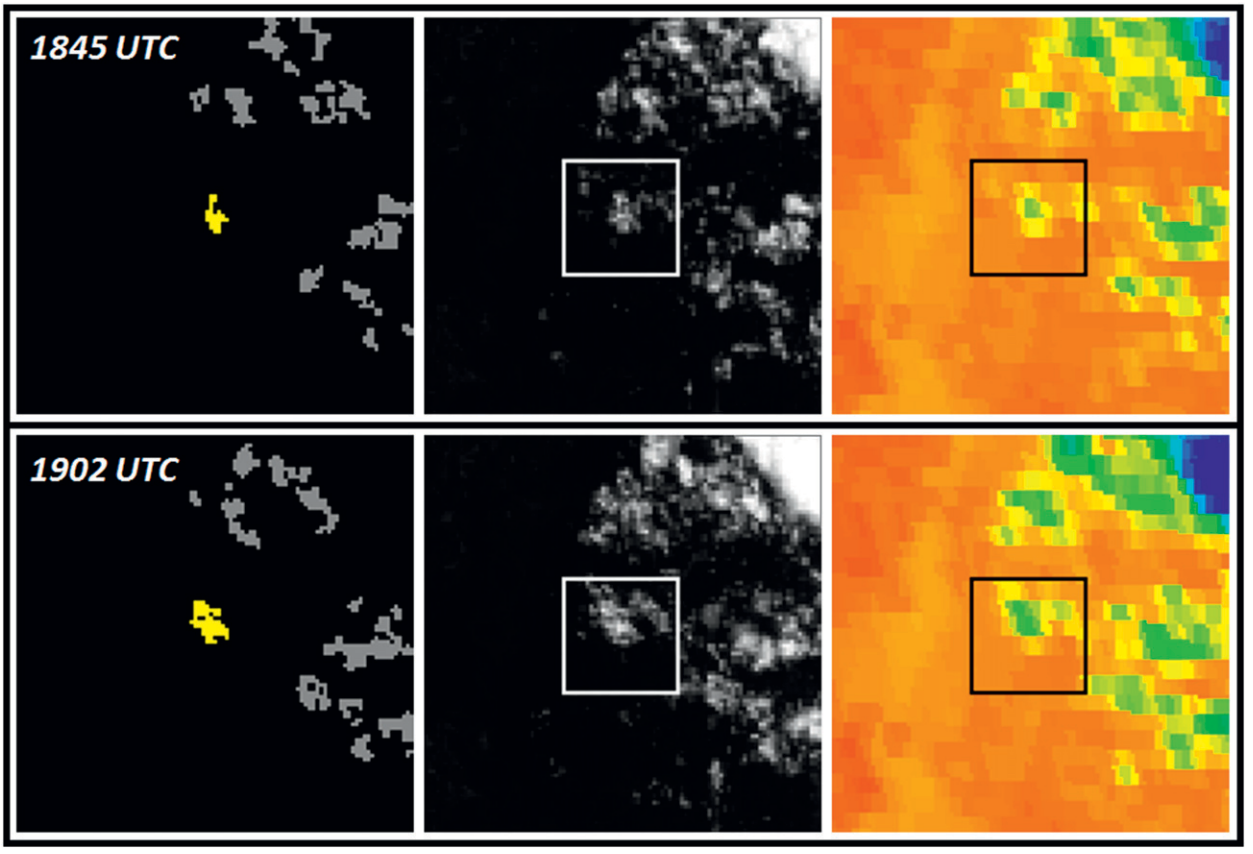

FIG. 1. For 7 Jun 2011 in southwestern Mississippi, (left) a single defined cloud object of interest (yellow) tracked from two consecutive satellite scans, (top) one at 1845 UTC and (bottom) the other at 1902 UTC, is shown. The corresponding (center) visible and (right) 10.7-μm IR *GOES-East* channels are shown for both times with a fixed 28 km $\times$ 28 km box (7×7 IR pixels of 4-km resolution) centered over a developing cumulus cloud to show the spatial extent to which pixel averaging is occurring when performing a box average. The object-tracking method described in this paper yields a 10.7-μm cloud-top cooling rate of -6.0 K (15 min)$^{-1}$ for this growing convective cloud, and the local-area average of cloud pixel T_Bs contained within the box yields a decreased cloud-top cooling rate of -0.4 K (15 min)$^{-1}$.

derivation, 3) CCM generation, 4) cloud-object tracking (OT), 5) spectral testing/interest-field calculations, and 6) CI forecast determination. These are described in order below. Note that, as of the writing of this paper, the SATCASTv2 algorithm is capable of processing input data and producing output CI forecasts within approximately 2.5 min of receiving the latest GOES data, using the computer processers and resources available at this time. Beyond that, testing has shown that distribution of the output to product users is accomplished in less than 1 min.

a. Acquiring satellite data

Satellite data from the *GOES-13* instrument is acquired regularly in real time, following the *GOES-13* routine scan operations for its continental-U.S. (CONUS) domain. As of 2010, the temporal resolution for the GOES data is typically ~15 min but can be as low as 30 min when the instrument is scheduled to perform a ''full disk'' scan of Earth. Also, the spatial resolution of this imager is 1 km for the visible channel and 4 km for the IR channels, at nadir. The algorithm requires an input of three consecutive GOES-image datasets, including all five available channels for each time (visible and 3.9, 6.5, 10.7, and 13.3 μm).

b. Deriving mesoscale atmospheric motion vectors

Once the latest satellite data have been acquired, a MAMV derivation code is used to discern cloud-pixel velocity. This MAMV algorithm (Bedka and Mecikalski 2005; Bedka et al. 2009) was developed for use in the original SATCAST algorithm for the single-pixel tracking. Once the MAMV processing is complete, the SATCASTv2 algorithm no longer has need for the first input satellite image and will require only the two most recent image datasets. Although the MAMVs derived from one triplet

of input satellite data are likely valid for periods as long as 30–60 min in most cases, it is prudent to rederive the vectors with each new satellite scan, given the quickly changing nature of cloud motion at the mesoscale, and especially when using such linear extrapolation techniques as are used for the given method.

c. Generating convective cloud masks

While the MAMVs are being generated, another part of the SATCASTv2 algorithm is used to create a CCM. The CCM code takes in all of the newly acquired satellite channels and employs a supervised classification scheme to produce an output-image array of integer-defined cloud types (Berendes et al. 2008). From this output, only those clouds that are deemed immature, or ''preconvective,'' in nature are retained for further processing, that is, cumulus, towering cumulus, warm water clouds, and cold water clouds. Later in the processing, pixels from these retained cloud types will be used to define input ''cloud objects'' in the object-tracking section of the SATCASTv2 algorithm. All other cloud types considered to be ''mature'' or nonconvective (such as thick ice cloud, cirrus, or stratus) are omitted.

The CCM algorithm is heavily dependent upon visible data for input, since the spatial texture information that this channel provides helps to distinguish between cloud types that have similar IR spectral signatures (Berendes et al. 2008). Because of this reliance upon visible satellite data, the initial version of SATCASTv2 is a ''daytime only'' algorithm. Subsequent versions will incorporate a nighttime cloud mask, thus making it a ''day/night algorithm.'' The current version of SATCASTv2 does well to capture the most active part of the diurnal convective cycle, the afternoon, which accounts for a large portion of all convective events in the United States (Easterling and Robinson 1985).

d. Tracking cloud objects

The main innovation in SATCASTv2 is the combined use of the derived MAMVs with the selected cloud-type output from the CCM to track the preconvective clouds, here referred to as ''cloud objects,'' between the two most recent input sets of satellite imagery. For the sake of simplicity, this couplet of satellite data is chronologically labeled for input time 1 (T1) and input time 2 (T2), where T2 is the newest data. This OT technique closely follows the method of Zinner et al. (2008), in which ''temporal overlap'' is required to facilitate the tracking of cloud objects from T1 to T2. To accomplish OT, first, each object (all corresponding 1-km pixels) from T1 is assigned a unique, positive integer identification number (IDN). Next, the MAMVs are prescribed to the nearest T1 cloud objects (Fig. 2a), such that all pixels belonging to a given object receive the same u and v wind components. Then, these adopted motion vectors are used to linearly advect each T1 cloud object to a forecast position that would correspond to its expected location at T2 (Fig. 2b) as based on the time difference between T1 and T2. In theory, if the cloud still exists at T2, then there should be overlap between the advected T1 cloud objects and the actual T2 cloud objects (Fig. 2c). Where this temporal overlap exists, the IDN that was assigned to a given T1 cloud object is passed on to the corresponding T2 cloud object (Fig. 2d). In doing so, a means of identifying the same clouds from two consecutive input satellite-image times is established; thus, cloud-object tracking is achieved.

e. Calculating interest fields

Once the OT scheme is complete, a series of spectral and temporal differencing tests, known as CI ''interest fields'' (Mecikalski and Bedka 2006), are performed on each cloud object. These interest fields are adopted from the original SATCAST algorithm (Table 1) and stem from several previous studies, as discussed above. They are used to diagnose certain physical properties of preconvective clouds that are relevant to the assessment of CI potential: 1) cloud-top height, 2) cloud-top glaciation, and 3) updraft strength.

Unique to SATCASTv2, to perform the spectral tests, representative T_Bs must first be selected for each cloud object, for all required IR channels, and for both input-image times, T1 and T2. To acquire these representative T_Bs, all pixels within each cloud object (mapped to a 1-km-resolution grid) are sorted from coldest to warmest for a given input time, according to the 10.7-μm spectral channel. Then the coldest 25% of pixels from each cloud object are averaged to derive a representative T_B for that channel. Because radiation detected by the 10.7-μm channel is subject to less absorption by atmospheric gases than is radiation detected by the other GOES IR channels, it is assumed that T_Bs from the 10.7-μm channel will yield a more accurate representation of the relative magnitudes of the temperature field across the tops of cloud objects. Therefore, by using this coldest 10.7-μm pixel subset the OT algorithm gains a better focus on the colder updraft regions within cloud objects (Harris et al. 2010), whereas using an average of all pixels within an object may lead to a blurring of the CI spectral signals and using the single coldest 10.7-μm pixel from each cloud object may introduce CI signal errors from possible satellite instrument noise. In situations in which a cloud object is composed of only a few pixels, however, the single coldest 10.7-μm T_B pixel is used as the representative subset for that cloud object. Once this per-object subset is established, the same subset of pixels is

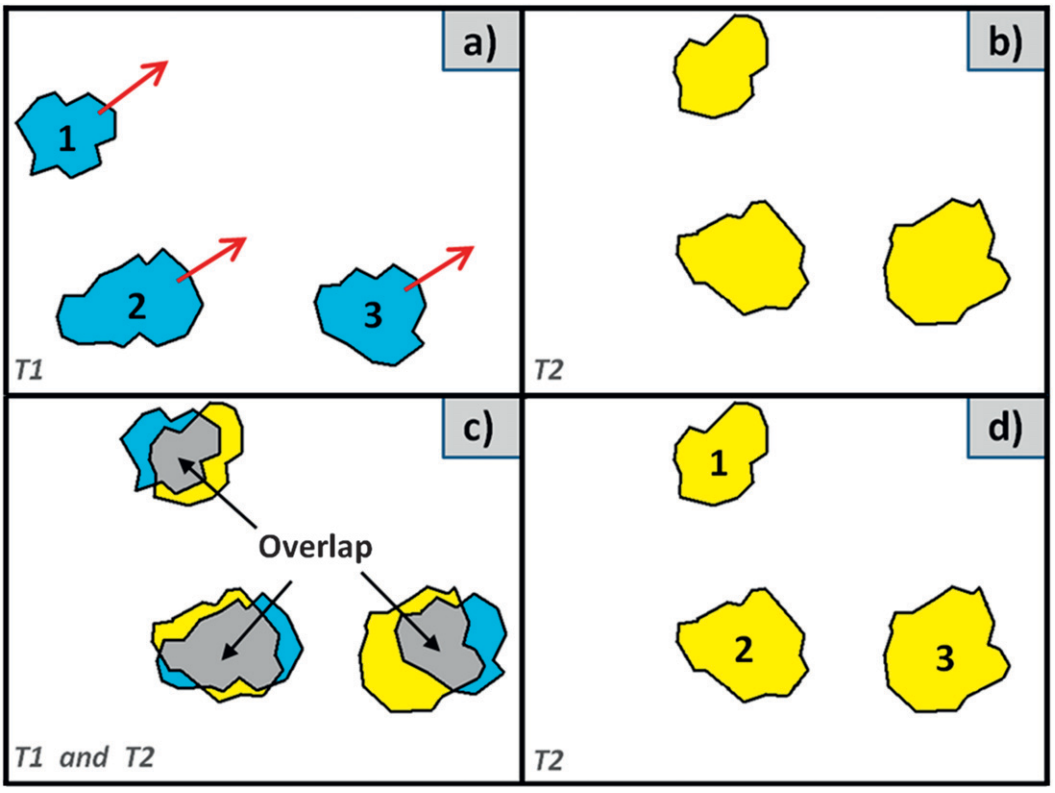

FIG. 2. Example of the cloud-object-tracking method. (a) First, each of the T1 cloud objects (blue) is assigned an IDN and prescribed a motion vector before being advected to a forecast-extrapolated position of where it would be expected at T2. Next, the positions of (b) actual T2 cloud objects (yellow) are (c) compared with those of the forecast advected T1 cloud objects. When temporal overlap exists, the IDNs assigned to the T1 cloud objects are (d) inherited by the corresponding overlapping T2 cloud objects, which completes the OT routine.

used to derive the representative T_B for all input IR channels. Then the process is repeated for the other input satellite data time (T2), and the calculation of CI interest fields can proceed.

Using the cold-pixel subset for CI interest-field calculation is of great benefit in situations involving "object merging." Object merging occurs when a single object from T1 closes the gap between one or more other objects and overtakes the object(s) at T2, essentially joining multiple objects into one (sometimes "webbed") contiguous object. An example of cloud-object merging would occur when a growing cumulus cloud, existing within a tightly clustered cumulus field, connects with and overtakes some of the surrounding clouds in the field. In that case, all pixels belonging to the resulting contiguous cloud object at T2 would inherit the unique IDN of the original overlapping cloud object from T1. Applying the cold-pixel-subset technique helps to focus on the actual growing cloud from T1 to T2 rather than on the surrounding, merged clouds contained within the T2 object. This approach ultimately produces a more accurate forecast of CI in the output.

f. Determining CI forecasts

Mecikalski and Bedka (2006) showed that, when a significant majority of the CI interest-field critical thresholds are met, CI is ~60% likely to occur within the next 0–2 h. Similarly, for the current GOES SATCASTv2 algorithm, five out of the six interest-field critical thresholds (from Table 1) must be met for a positive CI forecast

TABLE 1. List of CI interest fields developed for the operational *GOES-13* satellite instrument as used in SATCASTv2. Note that some of the interest fields are "static," incorporating satellite data from only the most recent scan time, whereas others use a temporal difference (also referred to as a "time trend") across the two most recent satellite scan times.

CI interest field	Critical value
10.7-μm T_B	0°C
10.7-μm T_B time trend	$\leq$[−4°C (15 min)$^{-1}$]
6.5–10.7-μm T_B difference	From −35°C to −10°C
13.3–10.7-μm T_B difference	From −25°C to −5°C
6.5–10.7-μm T_B time trend	>[3°C (15 min)$^{-1}$]
13.3–10.7-μm T_B time trend	>[3°C (15 min)$^{-1}$]

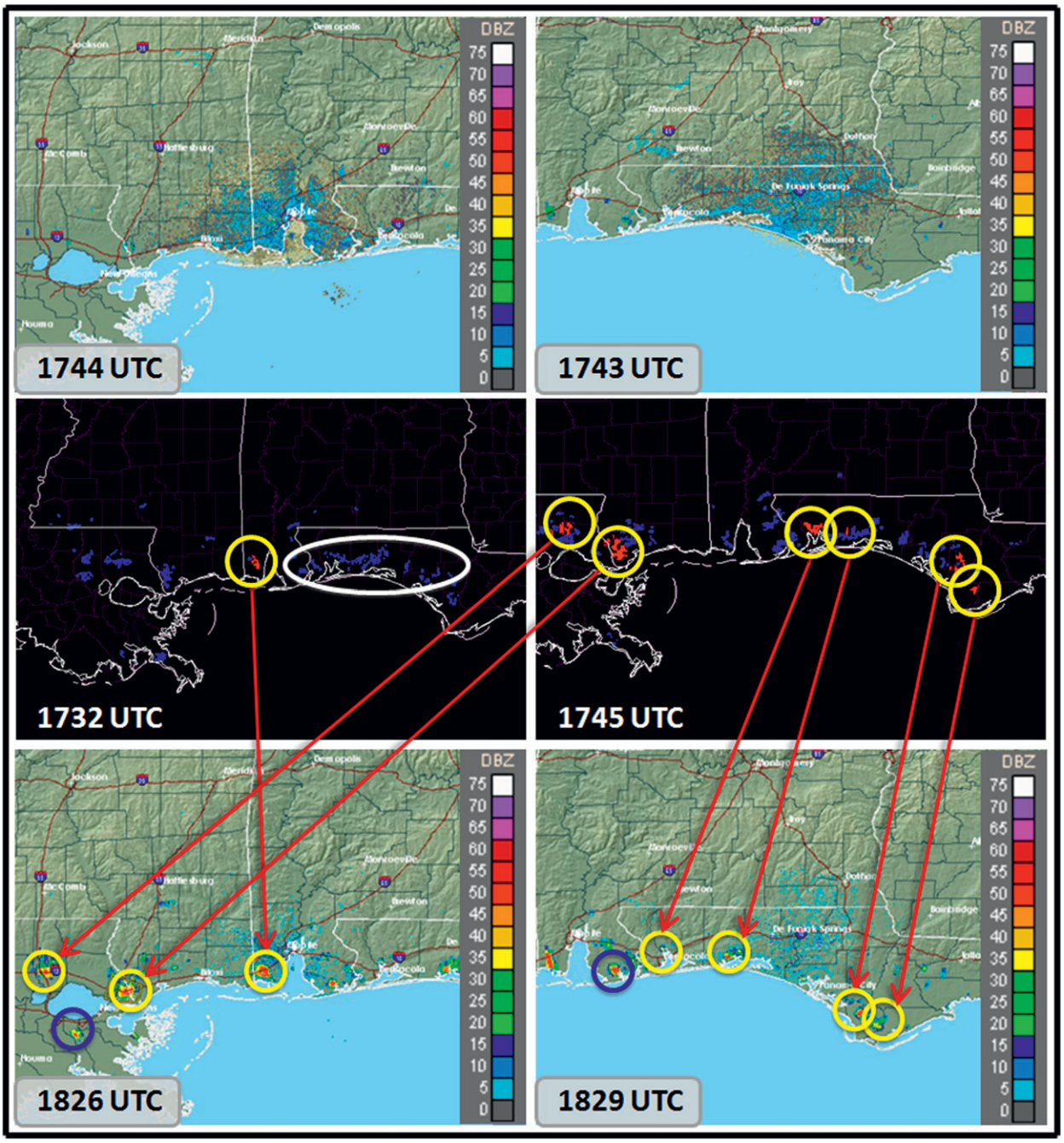

FIG. 3. Examples of the (middle) SATCASTv2 product output and validating WSR-88D 0.5° base-reflectivity radar data from (top left and bottom left) Mobile, Alabama, and (top right and bottom right) Tallahassee, Florida, from 6 Jun 2011 along the northern Gulf Coast. The red cloud objects indicate positive CI forecasts, for which at least five of the six interest field tests were passed, and the blue cloud objects represent the null forecasts, for which fewer than five interest field tests were passed. The yellow rings indicate correct positive CI forecasts (hits), and the blue rings indicate misses, where CI occurred but was not forecast. Note from the labeled time stamps that the first series of CI forecasts was generated prior to any indication of convection from the radar.

to be generated (Fig. 3). When fewer than five tests are passed, a ''null'' or negative forecast for CI is assigned for a given cloud object on the basis of information from the current couplet of input satellite images, indicating that the cloud object does not exhibit a strong-enough signal of cloud-top growth and placement to justify a positive forecast for near-future CI. It is possible for that same cloud object to obtain a positive CI forecast when

the next satellite image becomes available and the ''new'' couplet of image data is input into the algorithm (Fig. 4). Also, there are instances in which a series of forecasts may alternate from null to positive for the same cloud object, usually indicating that the cloud top is slowly growing (i.e., cooling) at a rate that is very close to the algorithm's critical thresholds.

It should be emphasized that the CI forecasts generated by SATCASTv2 are based solely on the very latest set of available satellite images and, in part, from the resulting T_B trends that are derived from no more than two points in time. SATCASTv2 incorporates *diagnostic* information such as the current cloud-top height, cloud-top glaciation, and updraft strength of potentially convective clouds. Its purpose, however, is to use this information to *infer* (from linear extrapolation) which immature cumulus clouds that are showing evidence of recent development will continue to grow into precipitating, mature convective storms. Therefore, the diagnostic assessment is utilized in such a way as to produce prognostic forecasts of likely CI events. There are instances in which this inference is incorrect, as when cloud growth ends before CI occurs.

4. Validation

a. Approach

Validation of SATCASTv2 was accomplished using a dichotomous forecast verification technique. To compute accurate statistics, a 2×2 contingency table was developed (Table 2). For our purposes, this contingency table was populated on the basis of the answers to the following two questions: 1) Did the algorithm predict the CI event? 2) Was the CI event observed? A CI forecast was categorized as a ''hit'' when the answer to both questions was ''yes,'' considering all positive CI forecasts. A CI forecast was categorized as a ''correct negative'' when the answer to both questions was ''no.'' These assessments considered null CI forecasts. Similarly, a ''false alarm'' was counted when the algorithm predicted a CI event but CI was not observed, and a ''miss'' was counted when the algorithm did not predict a CI event but an event was observed. Each of these instances was tallied in the contingency table for the calculation of validation statistics.

To fill the contingency table, each cloud-object CI forecast was compared with 0.5°-elevation-angle radar data up to 2 h in the future inside a domain that encircled a given radar site with a radius of ~75 km. This set radius was used in conjunction with the 0.5° radar elevation angle to ensure consistency and to make sure that no low-topped convective events were missed because of overshooting of the radar beam at greater distances from the radar site. Furthermore, using this 75-km radius helped to avoid the decreased resolution of radar data at farther distances from a site. The ≥35-dBZ precipitation-intensity threshold was determined from National Weather Service Weather Surveillance Radar-1988 Doppler (WSR-88D) base reflectivity for the determination of CI events, because this is a metric that is prominently found in the literature (Mueller et al. 2003; Roberts and Rutledge 2003; Mecikalski and Bedka 2006). The validation was approached subjectively to ensure high accuracy in the results and to avoid introducing errors that are inherent to an objective validation approach. Such errors that were avoided by employing a subjective validation technique had to do with the ease in determining which occurrences of ≥35-dBZ radar echoes were convective in nature, as opposed to stratiform or melting-layer radar echoes. Furthermore, the subjective approach allowed for simple identification of new CI events without confusing them with ongoing convective storms, which would have been another difficult problem to overcome in an objective validation approach.

Once the contingency tables were populated, statistics were computed. A list of the statistics developed for this study can be found in Table 3. The validation study was conducted over four independent regions across the CONUS during the spring/summer of 2010. These four regions were selected on the basis of the unique convective regimes existing within each area. The purpose for such a diversified selection was to determine the potential presence of any convective regime bias within the algorithm, with regard to any significant differences in the CI forecast output. For each case day, all CI forecasts, both positive and null, that were available within the preset radial domains were included in the study. In total, 9943 cloud-object CI forecasts were validated. The associated performance statistics from this validation effort of the first seasonal preliminary run of the SATCASTv2 algorithm are shown in Tables 4 and 5. The four regions used to conduct the validation encompass the following locations:

1) Melbourne, Florida—This validation period ranged from 1 to 3 June 2010, and the convective regime was characterized by tropical convection and sea-breeze thunderstorm activity. The Melbourne radar site was used for truth data. A total of 2010 CI object forecasts were validated, and 262 CI events were considered.
2) Memphis, Tennessee—This validation period ranged from 24 to 25 May 2010, and the region was dominated by general ''airmass'' thunderstorm activity. The Memphis radar site was used for truth data, and

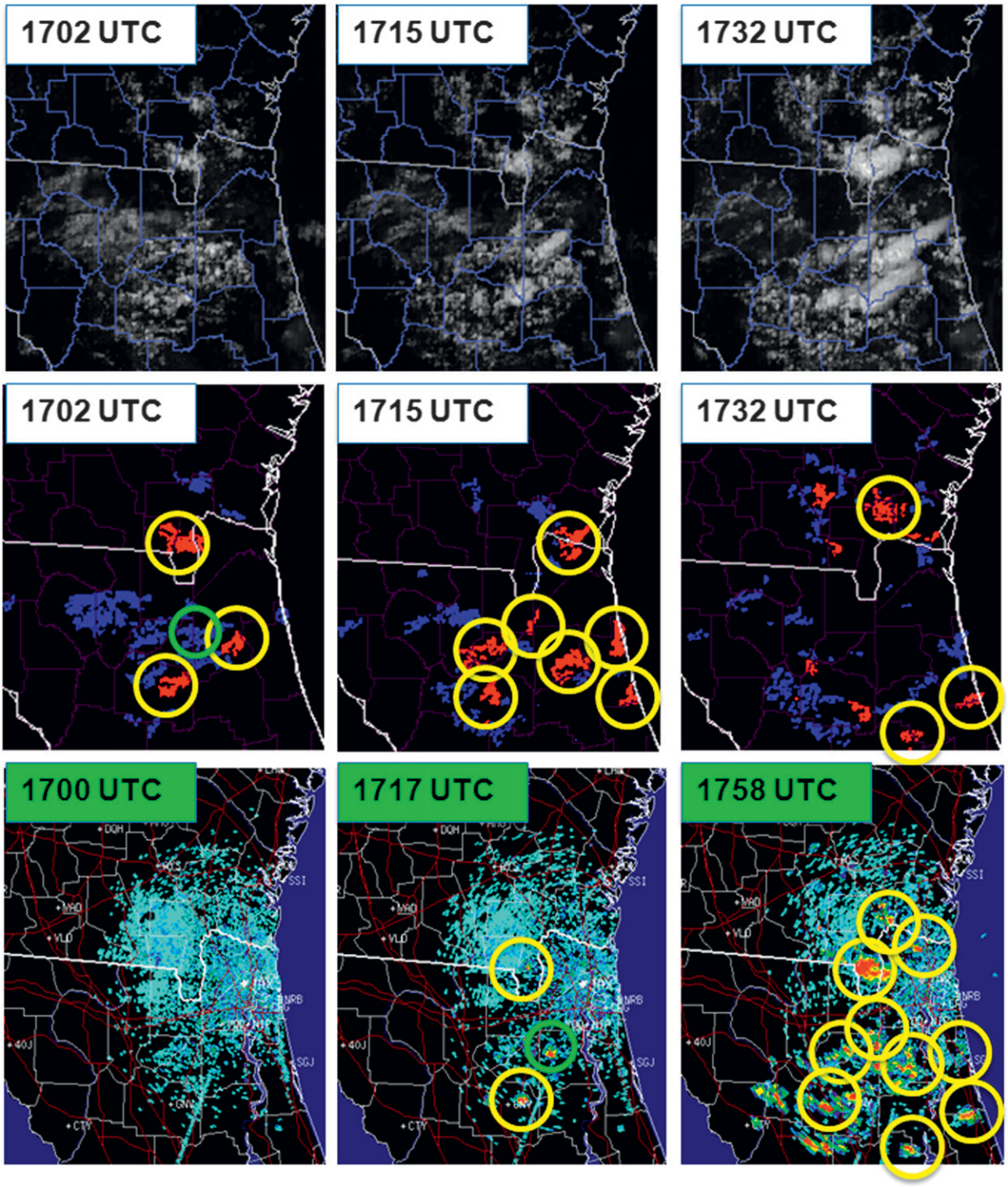

FIG. 4. Examples of (middle) SATCASTv2 output, accompanied by corresponding (top) visible satellite data and (bottom) validating WSR-88D 0.5° base-reflectivity radar data from Jacksonville, Florida, from 6 Jun 2011 over northern Florida and southern Georgia. The yellow rings indicate hits, and the green rings indicate a miss. Note from the labeled time stamps that the first series of CI forecasts was generated prior to any indication of convection from the radar. Also, note that some of the cloud objects that originally produced null CI forecasts generated positive CI forecasts in subsequent outputs of the product.

TABLE 2. Dichotomous forecast verification contingency table used to calculate validation statistics for this study.

	Obs = yes	Obs = no
Forecast = yes	Hits (H)	False alarms (FA)
Forecast = no	Misses (M)	Correct negatives (CN)

829 CI object forecasts were validated, with 212 CI events considered. There were fewer forecasts validated for this region because widespread cirrus contamination prevented the algorithm from generating many forecasts.

3) Central United States/Great Plains—This validation period occurred on 16 July 2010. The environment was highly unstable [surface-based convective available potential energy (SBCAPE) of 3000–6000 J kg^{-1} across the domain], with several reports of severe weather in the form of large hail and damaging wind from thunderstorms. The radar sites used for truth data were Springfield, Missouri; Wichita, Kansas; Topeka, Kansas; Kansas City, Missouri; and Omaha, Nebraska. A total of 4275 CI object forecasts were validated, with 203 CI events found.
4) Northeastern United States—This validation period ranged from 26 to 27 June 2010 and was characterized by a quickly transitioning convective environment, as multiple shortwave troughs propagated across the region around a larger upper-level trough located to the north. The radars used for truth data were Cincinnati, Ohio; Cleveland, Ohio; Detroit, Michigan; and Pittsburgh, Pennsylvania. A total of 2829 CI object forecasts were validated, and 127 CI events were considered.

As of the writing of this paper, the SATCASTv2 algorithm has not yet been implemented using data from the *GOES-11/West* satellite. Once this is accomplished at some future date, it is hoped that a full season of convection can be observed and validated within the algorithm over the mountain regions of the western United States. The scarcity of available radar data for verification purposes in that region will be an issue that will have to be addressed when that time arrives.

TABLE 3. List of statistical equations that were derived from the forecast verification contingency table and were used to quantify the performance of the version of the SATCASTv2 algorithm used for this study. The acronyms POD, POFD, and FAR are defined in section 4b.

POD	$H/(H + M)$
False-alarm rate, or POFD	FA/(FA + CN)
FAR	FA/(FA + H)
Accuracy	$\frac{(H + \mathrm{CN})}{(H + \mathrm{CN} + M + \mathrm{FA})}$

TABLE 4. Contingency tables generated from the forecast output from the SATCASTv2 algorithm for all study regions, broken into three classes of statistical evaluation. The four cells below each class label correspond to the quadrant structure of the contingency table diagram in Table 2; that is, the top-left cell is H, the bottom-left cell is M, the top-right cell is FA, and the bottom-right cell is CN. Note that only the number of misses M changes for each class. "Class 1" relates to all CI forecasts and corresponding CI events that were associated only with "tracked cloud objects," and class 2 represents all CI events documented in the validation study, whether or not they were associated with algorithm output forecasts, with the exception of those masked or affected by cirrus contamination. Class 3 represents all documented CI events for this validation study, including those that occurred beneath thick cirrus clouds as well as those that were not associated with any algorithm forecast output.

Class 1		Class 2		Class 3	
255	308	255	308	255	308
99	9281	190	9281	549	9281

b. Results and discussion

The contingency tables and statistics are broken into three classes. Class 1 relates to all CI forecasts and corresponding CI events that were associated only with "tracked cloud objects" [first column(s) of Tables 4 and 5]. In other words, this class considers only those CI events that had any forecast (positive or null) associated with them, ignoring unrelated misses that resulted from cirrus contamination and the inability to track cloud objects because of the low temporal resolution of the current GOES instrument. These statistics help to gauge how SATCASTv2 actually performs when it can track accurately—a task more easily accomplished with higher-temporal-resolution data—and therefore can evaluate the properties of cloud objects, although errors still exist in this subset (see section 5). In this respect, more emphasis can be placed on the combination of cloud OT and multispectral differencing techniques that are central to the SATCASTv2 algorithm.

TABLE 5. Validation statistics and averaged lead times from the referenced version of the SATCASTv2 algorithm for all study regions, broken into the three classes of statistical evaluation. Note that only the POD and accuracy statistics change for each class. See Table 4 for definitions of the three classes listed.

	Class 1	Class 2	Class 3
POD	72%	57%	32%
POFD	3%	3%	3%
FAR	55%	55%	55%
Accuracy	96%	95%	92%
Lead time (min)	29.6	29.6	29.6

The second class of statistics (class 2) represents all CI events documented in the validation study, whether or not they were associated with algorithm output forecasts, with the exception of those masked or affected by cirrus contamination [middle column(s) of Tables 4 and 5]. The only difference between class 1 and class 2 is that the number of misses is greater in the second class of statistics, which are the result of CI events that occurred with no related CI forecasts in the vicinity. A comparison between class 2 and class 1 shows the need for higher-temporal-resolution satellite data input for SATCASTv2 for the purpose of tracking cloud objects. If the clouds cannot be tracked, no forecasts can be made, and the result is more CI events that occur with no associated CI forecasts.

The class-3 set of statistics represents all documented CI events for this validation study, including those that occurred beneath thick cirrus clouds as well as those that were not associated with any algorithm forecast output [last column(s) in Tables 4 and 5]. These values take into account all possible limitations, and by comparison with the other two sets of figures, show how detrimental cirrus obstruction is to nowcasting CI using a satellite-based system.

Note that only the probability of detection (POD) and the accuracy actually change across all three classes of statistics, since these are the only values that are affected by misses. In addition, the accuracy remains >90% for all classes; this elevated level of performance is, however, largely due to the high number of correct negative forecasts tallied, as seen in the contingency tables. For the same reason, the probability of false detection (POFD), also referred to as the false-alarm rate, is very low at 3%. In essence, when the algorithm produces a null forecast, there is a very high likelihood that no associated CI will be observed in the near future. It is worth noting that the contingency-table numbers were the result of all generated forecasts for the entire study period within the preset domains and were consequently selected without bias. Also, only convectively active days were considered for this study. Thus, there was no artificial inflation in the number of correct negatives. As can be observed on any typical convectively active day, the large majority of pre-CI cumuliform clouds that were found within the study domains simply did not develop into mature convection (~96.4%), leaving a relatively small subset that did lead to CI. Therefore, since this is a cloud-object-based algorithm, it is important to consider all individual CI forecasts when evaluating its performance, even the null forecasts, as long as the other performance statistics are also considered.

Although the accuracy changed little for each class of performance values, the statistic that was most negatively affected in the succession of classes was the POD. Starting at 72% in class 1, the POD dropped to 57% when non-forecast-related misses were considered in class 2, and it dropped further to 32% when cirrus-masked misses were also considered in class 3. Once again, the added misses in class 2 can be explained mainly by the difficulty in properly tracking clouds when using satellite data with temporal resolutions of 15–30 min. From the class-3 POD, it is evident that cirrus contamination has the most profound negative effect on the ability of SATCASTv2 to produce CI forecasts.

Also included in the list of statistics is the average lead time (Table 5) that was calculated for all hits. The average CI forecast lead time for 35-dBZ echoes was ~30 min, with a median value of 26 min, when all study domains were considered, and it ranged anywhere from 0 min (termed a ''diagnostic'' forecast with no added value over radar data) to up to ~2 h for a few extreme cases. To maintain consistency, the lead time for each hit was calculated as the difference between the satellite-image time stamp of the most recent input GOES image and the radar time of the corresponding CI event.

It is clear that one of the main issues associated with the SATCASTv2 algorithm is the number of false alarms. With an average false-alarm ratio (FAR) of 55% for all study domains, there is much room for improvement. Many of the problems leading to the high FAR are identified in the following section, including potential errors in cloud OT, issues with thin-cirrus contamination, and problems with new cumulus development. Manual testing of the CI interest fields, with the omission of automated cloud OT, has shown that a significant number of CI-forecast false alarms are eliminated when applying the multispectral differencing techniques used in the SATCASTv2 algorithm, when compared with other techniques that use only the 10.7-μm cooling rate for nowcasting CI events (Walker and Mecikalski 2011). Research is ongoing toward decreasing potential sources of error within the algorithm while increasing the accuracy of the automated cloud OT method. It is believed that this will effectively reduce the FARs for SATCASTv2 while helping to preserve or increase the POD statistic.

To identify potential variations in the algorithm performance as a result of regional and environmental differences, the statistics were also tallied for each of the four regional study domains (Table 6). From Table 6, it is evident that the algorithm performs most poorly in the tropical environment of coastal Florida, where the shortest lead times and lowest PODs are found. The reduced average lead times (~24 min) are related to previous findings that growing clouds in these types of warm tropical regimes are very efficient at producing

TABLE 6. Validation statistics and averaged lead times from the referenced version of the SATCASTv2 algorithm, broken into the three classes of statistical evaluation for each of the four study regions. Once again, note that only the POD and accuracy statistics change for the different classes. See Table 4 for definitions of the three classes listed.

	Melbourne			Memphis			Central United States/ Great Plains			Northeastern United States		
	Class 1	Class 2	Class 3	Class 1	Class 2	Class 3	Class 1	Class 2	Class 3	Class 1	Class 2	Class 3
POD	54%	43%	21%	74%	45%	24%	85%	78%	46%	75%	67%	44%
POFD	4%	4%	4%	6%	6%	6%	3%	3%	3%	2%	2%	2%
FAR	60%	60%	60%	48%	48%	48%	55%	55%	55%	54%	54%	54%
Accuracy	94%	92%	87%	92%	87%	78%	97%	97%	95%	97%	97%	95%
Lead time (min)	23.8	23.8	23.8	32.7	32.7	32.7	32.9	32.9	32.9	27.4	27.4	27.4

heavy precipitation (Li et al. 2002) and, therefore, do so more quickly than in other environments. Because of the generalized global critical thresholds used in the CI interest-field tests in the current SATCASTv2 algorithm, several of the growing cloud objects in this study did not exhibit vigorous enough growth to trigger positive CI forecasts, yet vigorous vertical growth was not necessary for the clouds to produce a ≥35-dBZ radar echo, resulting in a number of missed forecasts. This finding is substantiated when the PODs from the Melbourne study region are compared with those from the Memphis region. The stability profiles for these study domains were similar, both possessing a significant amount of SBCAPE (1000–3000 J kg^{-1}) and a general lack of inhibition (CIN) (<25 J kg^{-1}), yet the Memphis environment was nontropical in nature. The class-2 and class-3 POD statistics are very similar, indicating that a comparable number of misses resulted from the inability of the algorithm to track the CI-related cloud objects for various reasons stated above. At 74%, the class-1 POD statistics are significantly higher for the Memphis domain than in the Melbourne domain, where the class-1 POD is at 54%. This would indicate a significant difference in the number of missed CI forecasts for all *tracked* cloud objects between the two study domains. In this situation, the CI interest-field global thresholds used in SATCASTv2 certainly proved much more beneficial in the Memphis domain than in the Melbourne domain, where many more misses resulted for the tracked cloud objects.

Out of the four study domains, the overall best performance statistics across all classes exist for the central U.S./Great Plains region. Although the FARs and POFDs here are comparable to the other regional statistics, this domain yielded the highest PODs in tandem with the longest lead times. Because the convective cloud development is usually more vigorous in such convective regimes, the pre-CI signals are stronger, making them easier for SATCASTv2 to identify (i.e., clouds in this type of environment are usually growing very quickly, exceeding all critical thresholds and making detection of future CI less difficult). For this region, most false alarms occurred when low-level clouds exhibited short-lived rapid growth until they reached the height of the midlevel capping inversion. Nevertheless, when the clouds were growing, either before or after the erosion of the capping inversion, they were usually growing at significant enough rates to trigger positive CI forecasts, resulting in a greater number of hits.

If one considers only the class-2 POD statistics, the algorithm performed significantly better in both the central U.S./Great Plains and in the northeastern U.S. domains (78% and 67%, respectively), as compared with the Melbourne and Memphis regions (43% and 45%, respectively). This signifies that the number of misses resulting from untracked cloud objects (i.e., nonforecasts) was much lower in the two formerly mentioned validation domains, and it indicates an improved ability of the cloud OT scheme to perform in those associated environments. This finding is further substantiated by the strong similarities in class-1 statistics (for tracked-only cloud objects) between the Memphis and northeastern U.S. study regions. That the statistics are so alike in class 1 but so different in class 2 in these domains shows that the multispectral approach yields similar results for all tracked cloud objects in these two study areas but that the main difference lies in the number of misses resulting from the inability to track as many clouds in the Memphis domain. The decreased performance of the cloud OT scheme in the Melbourne and Memphis study regions may be a direct result of the need to use global NWP forecast winds as a first guess for the derived MAMVs, used to facilitate cloud OT. The average 0000 UTC 700-hPa wind speed (a typical pressure for cumulus cloud tops in this study, as output from the MAMV algorithm) across the central U.S./Great Plains and northeastern U.S. domains was ~13.1 m s^{-1}, whereas the average 0000 UTC 700-hPa wind speed across the Melbourne and Memphis domains was ~5.4 m s^{-1}. Previous studies have shown that NWP models have a reduced accuracy

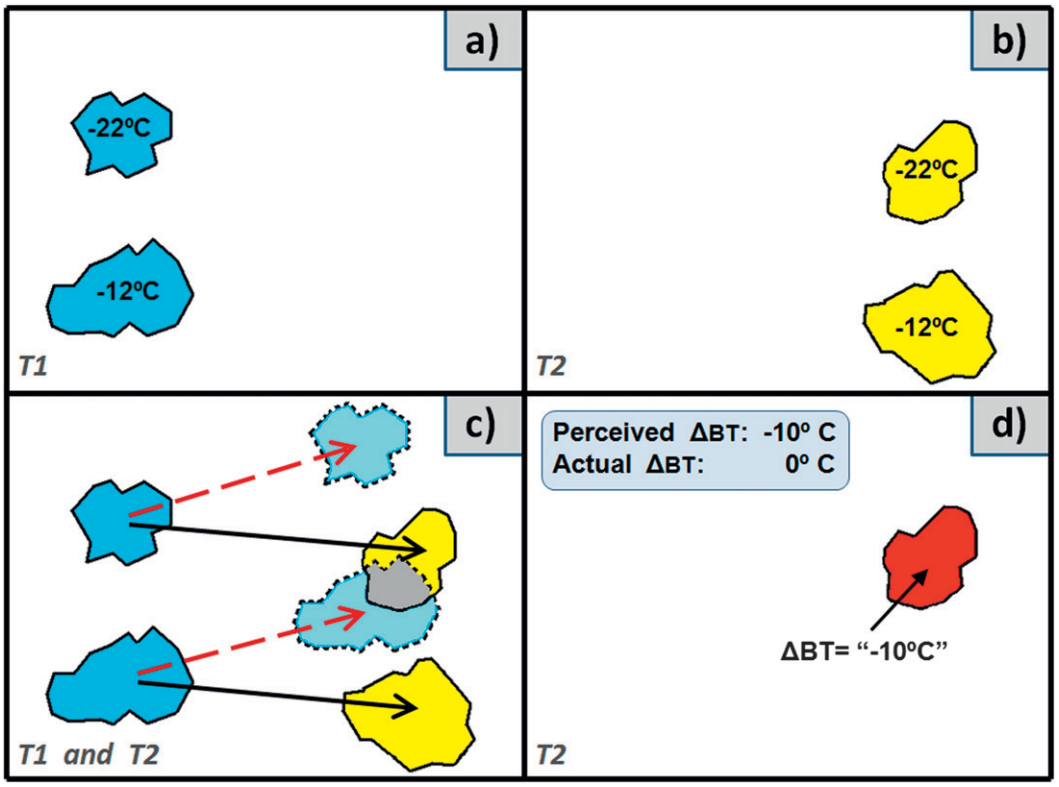

FIG. 5. Example of false tracking of cloud objects. (a) Blue polygons represent two cloud objects from T1, and (b) yellow polygons represent the same two cloud objects at T2. (c) Dashed red arrows and blue-shaded cloud objects indicate false vectors and resulting time-extrapolated displacement of T1 objects to expected positions at T2, while solid black arrows and yellow-shaded cloud objects indicate true motion vectors and actual locations of T2 cloud objects. The gray-shaded area represents overlap between an extrapolated T1 cloud object and an actual T2 cloud object. (d) The 10.7-μm T_B trend between the T1 and T2 images is actually 0°C for both cloud objects; because of false tracking, however, the perceived 10.7-μm T_B trend is -10°C for one of the cloud objects.

in forecasting lighter winds in less synoptically active environments (Engel and Ebert 2007; Huang et al. 2008).

5. Potential sources of error

Although the theory behind the SATCASTv2 algorithm is sound in its approach to monitoring cloud-top characteristics for the purpose of CI nowcasting, there are potential sources of error that are inherent to any such operational forecast algorithm. These errors mainly originate from problems in cloud OT and in situations related to cirrus-cloud contamination and subresolution initial cloud development, and these are discussed below.

a. Cloud OT errors

Two main potential causes of error in the SATCASTv2 algorithm are related to the cloud OT routine. The first one occurs as a result of false tracking, when small inaccuracies in the local MAMV field cause a cloud object from T1 to be mistakenly attributed as the same cloud object at T2 (Fig. 5). This error will affect none of the static CI interest-field calculations, those that use only the latest satellite data from T2; all of the calculations from the temporal trend tests (see listed items of CI interest field tests in Table 1 containing references to time trends) will be incorrect, however. Sometimes, if the two clouds that are mistakenly identified as the same cloud object are similar enough in cloud-top characteristics, then the resulting output of the algorithm is effectively unaltered. Yet, in other situations, as is the case in Figs. 5a–d, the output CI forecast for the cloud object is either mistakenly positive or mistakenly null. This, in turn leads to an increase in false alarms or an increase in misses, respectively. The current cloud OT method greatly mitigates tracking errors when compared with the original SATCAST single-pixel tracking method, but not all tracking errors can be eliminated. In the given example, the cloud objects at the top in Figs. 5a and 5b are the same, with a representative 10.7-μm T_B of -22°C that does not change in the time elapsed between images.

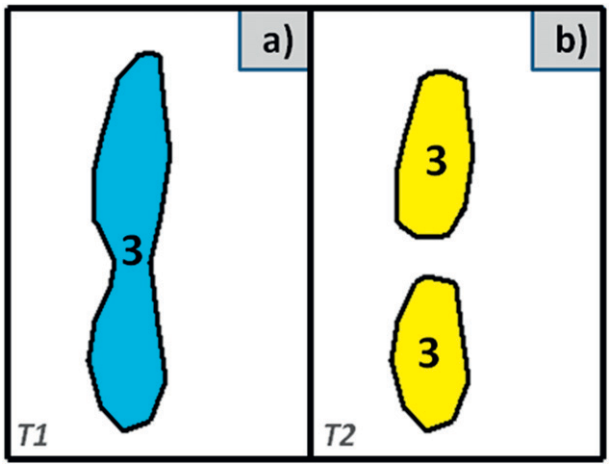

FIG. 6. Example of cloud-object splitting, resulting in (a) one cloud object at T1 with a given IDN—the number 3 in this case—and (b) two or more cloud objects at T2 with the same IDN. Both cloud objects at T2 will receive the same CI forecast, be it positive or null.

This is also true for the cloud objects at the bottom in Figs. 5a and 5b that have a representative 10.7-μm T_B of -12°C. In Fig. 5c, the dashed red arrows and resulting placement of time-extrapolated T1 cloud objects are the result of erroneously derived MAMVs, whereas the solid black arrows indicate the true vectors and placement of T2 objects. Because there is significant overlap between one of the time-extrapolated T1 cloud objects and one of the actual T2 objects, the algorithm concludes that the two cloud objects are the same in T1 and in T2. As a result, the temporal-trend CI interest fields will yield false calculations. In this case the 10.7-μm T_B trend shows a -10°C cooling rate between T1 and T2 for one of the cloud objects, and the algorithm completely ignores the other cloud objects that were not tracked (Fig. 5d). In fact, there should be two tracked cloud objects present, neither of which has a cooling cloud top.

The second potential error that could originate in the cloud OT routine is when a single cloud object from T1 is broken into two or more cloud objects at T2. Although rare, there are instances, usually associated with elongated cloud objects, when a gap forms between the cloud-filled pixels of a cloud object between consecutive satellite images, essentially splitting one cloud object into two. Because of the way that the cloud OT routine is designed to handle cloud-object merging, which is much more common than splitting, the result is two or more cloud objects at T2 ending up with the same IDN as the original single cloud object from T1 (Fig. 6). Using the coldest subset of pixels from the tracked objects, as described above, will help to provide a more accurate CI forecast in the end; this same forecast will be applied to all corresponding T2 objects possessing the same IDN, however. So, if one *accurate* positive CI forecast is generated in this situation, then one correct "hit" will be tallied for the statistics, but all of the duplicate forecasts will most likely fall into the false-alarm category. Similarly, if one *inaccurate* positive CI forecast is generated, then there would be multiple instances of false alarms counted in the statistics. Therefore, the resulting validation statistics will become negatively skewed as a result of such errors in cloud OT.

b. *Errors from cirrus-cloud advection*

Although "cirrus cloud" is one of the cloud types that is explicitly classified in the CCM and omitted from processing, there are many situations in which high, thin cirrus, sometimes found to be advecting outward from the edge of a mature cumulonimbus cirrus shield, escapes proper identification. In the algorithm, if the CCM does not detect the presence of such a cirrus deck, then it assumes that only the low-level clouds exist and processes the cloud objects accordingly. When this happens, the spectral signatures of the low-level clouds are distorted, making them appear cooler, with higher cloud tops than actually exist. This is a result of the satellite instrument sensing radiance contributions that are emitted, both from the low-level clouds *and* from the high-level thin cirrus for the same geographic location (Chang and Li 2003).

Such occurrences may adversely affect the quality of the CI forecast output. For example, if there is an immature cumulus cloud that is correctly tracked by the algorithm from T1 to T2, with *no* actual vertical growth, undetected cirrus contamination could cause the algorithm to incorrectly diagnose significant growth of this low-level cumulus cloud. This would happen if the cirrus cloud is advected over the cumulus cloud after T1 and is still located overhead at T2. Then, the satellite-sensed representation of the cumulus cloud would be significantly altered. Because the T_Bs from all IR channels would be would be significantly lower for the cloud at T2, all of the temporal trend CI interest fields would provide calculations that indicate the cumulus cloud top cooled and grew vertically, and the algorithm would likely produce a positive CI forecast that would result in a false alarm. It is extremely difficult to objectively identify such thin cirrus clouds, because of their optically thin nature (Saunders 1986), yet the best way to eliminate such CI forecasting errors is to improve the detection of these clouds.

c. *Errors from subgrid cloud growth*

Another cloud-related CI forecast error that can occur within this algorithm has to do with the development

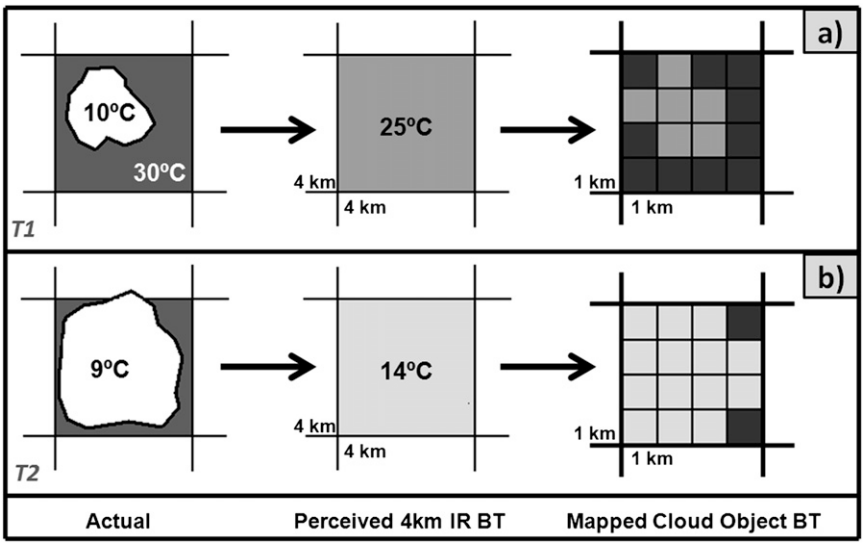

FIG. 7. Illustration showing how subresolution newly developing clouds may be erroneously perceived as possessing rapidly cooling cloud tops in the CI algorithm because of the 4-km spatial resolution of the *GOES-13* IR channels. (a) At T1, the actual cloud-top 10.7-μm T_B of a newly detected developing cumulus cloud is 10°C (left image) with an underlying surface T_B of 30°C, yet the 10.7-μm IR channel perceives a T_B of 25°C (middle image). (b) By the next satellite scan, at T2, the cloud has developed in horizontal extent (left image), but the cloud-top T_B has only actually cooled by 1°C. The satellite-perceived T_B for this channel is now 14°C (middle image), however, which the CI algorithm would interpret as a >10°C cooling rate for this particular cloud object, mapped back to a 1-km resolution [right images in (a) and (b)].

of new pre-CI clouds at horizontal sizes below the spatial resolution of the IR channel sensors, which would be 4 km × 4 km at nadir for *GOES-12–15*. As new clouds form, they are often detected and classified by the CCM in the early stages of development, since the CCM incorporates the 1-km visible-channel data from GOES as a primary input. When these early-stage cumuliform clouds are detected, however, they usually do not have enough horizontal width required to fill a full 4 km × 4 km IR pixel. The result is a set of T_Bs that are derived from a combination of radiances that originate both from the tops of small clouds and from the surface (Fig. 7). As these clouds continue in their initial stage of development between satellite-image scans, usually growing in width much more so than in height, they soon begin to fill the IR pixels. Since this limits the amount of surface-emitted radiation detected by the satellite sensor for a given pixel and concurrently increases the detected amount of cooler, cloud-top-emitted radiation, the perceived T_Bs are reduced in the algorithm for those cloud objects. The algorithm would interpret this signal as rapid vertical cloud development, and a positive CI forecast would likely be generated. Although newly formed clouds rarely progress immediately into mature convective clouds and thunderstorms, it does happen in environments for which the SBCAPE is high and the CIN is low or nonexistent. For the more common scenario mentioned above in which CIN is often prevalent and IR pixel filling is the case, however, a positive CI forecast is usually the result, which is generated for the wrong reasons and typically leads to false alarms.

d. Detection of vertical cloud development beneath capping inversions

The high FAR scores from SATCASTv2 are a notable concern, although sometimes they are the product of *correctly* detected vertical cloud growth prior to being inhibited from further development as a result of mid-level capping inversions. Despite being ultimately incorrect, in some cases these false-alarm forecasts can actually be used by a forecaster to increase situational awareness of an eroding capping inversion in advance of CI. Shown in Fig. 8 is an example of such an event. A sounding from Lincoln, Illinois, at 1200 UTC 24 May 2011 is included (Fig. 9), showing a weak inversion between 700 and 790 hPa, which acted to suppress CI over this region until after 1715 UTC.

From Fig. 8, SATCASTv2 forecast output is shown every ~15 min from 1602 to 1745 UTC, with accompanying radar spanning the time 1630–1815 UTC. Note

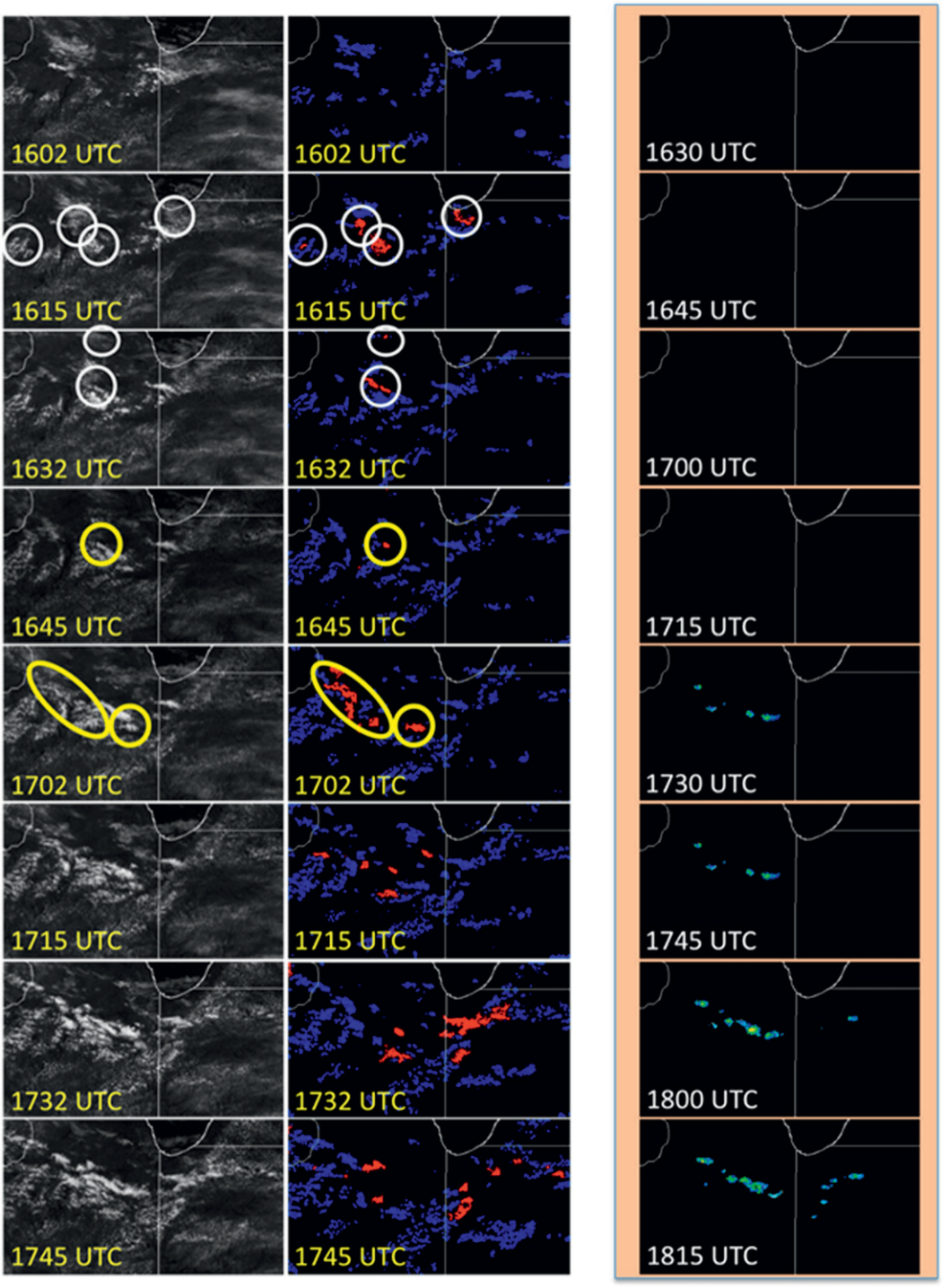

FIG. 8. (left) GOES 1-km visible-imagery, (center) SATCASTv2 output nowcasts, and (right) Next Generation Weather Radar (NEXRAD) radar reflectivity (dBZ) valid at the −10°C level, for the times listed on 24 May 2011. Note that SATCASTv2 objects pertain to CI occurrences 30–45 min into the future, and hence the satellite and radar data are offset by ~30 min in this example. For the SATCASTv2 images, red objects are CI "positive CI nowcasts" and blue objects are "null CI nowcasts." The NEXRAD echo intensities become yellow when greater than 35 dBZ. The CI nowcast false alarms are shown as white circles at 1615 and 1632 UTC, whereas yellow circles are correct nowcasts, shown until 1702 UTC. For a situational-awareness tool, SATCASTv2 provides indication that the capping inversion (see Fig. 9, described below) is weakening across northern Illinois, as the false alarms precede actual CI by 75 min (1615 vs 1730 UTC, when the first radar echoes are seen). The CI forecasts produced on or after 1645 UTC are mostly correct, with fewer false alarms. See the text for further description.

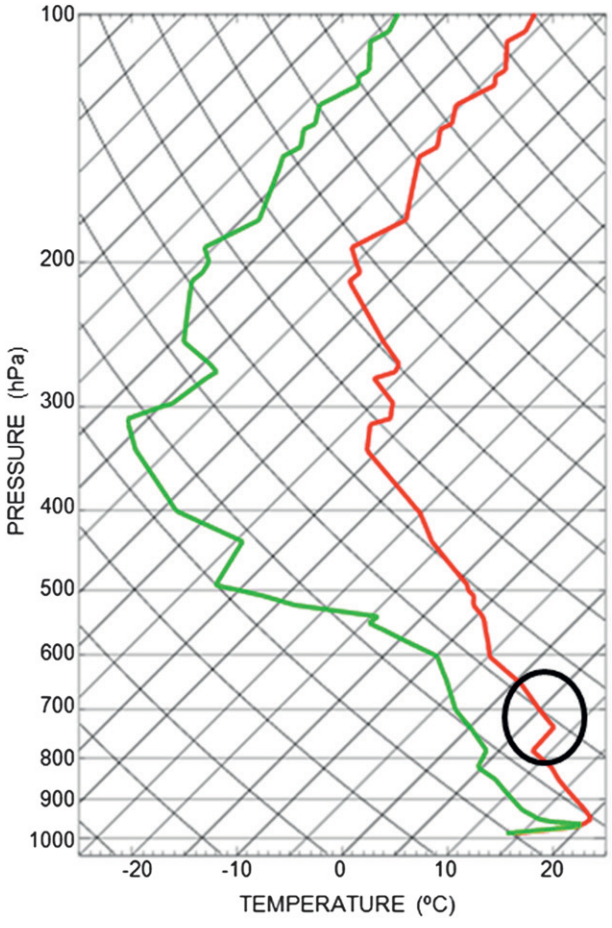

FIG. 9. Sounding at 1200 UTC 24 May 2011 for Lincoln. The environmental temperature is defined by the red line, and the dewpoint temperature is defined by the green line. A midlevel temperature inversion is highlighted by the black circle over the temperature trace, which exists from approximately 700 to 790 hPa.

that CI forecast "hits" identified by SATCASTv2 are verified as ≥35-dBZ radar echoes ~30–45 min into the future, downstream as the clouds move (viz., east in the example). These first radar echoes appear at 1730 UTC, which correspond to the positive CI forecasts from the 1645 and 1702 UTC SATCASTv2 output images. In the forecast output preceding 1645 UTC, however, the FARs (white-circled red cloud objects) can be used to highlight locations where convective development is gradually weakening the capping inversion. After 1730 UTC, a high spatial correlation exists between SATCASTv2-identified CI nowcasts and 30–45-min radar echoes >35 dBZ in intensity, as storms developed across Illinois and Indiana. In this situation, SATCASTv2 provides indication that the capping inversion (see Fig. 9) is weakening across this region, as the false alarms precede actual CI by 75 min (1615 versus 1730 UTC, when the first radar echoes are seen). CI forecasts that are produced onward from 1645 UTC are mostly correct, with significantly fewer false alarms.

6. Conclusions

This study demonstrates the utility of an OT approach within SATCASTv2, a 0–2-h CI nowcasting algorithm, and subsequently provides validation statistics to demonstrate the method's skill at forecasting new CI. The OT approach used in SATCASTv2 is a modified form of that presented in Zinner et al. (2008). We propose that cloud OT is a physically consistent way of monitoring for CI, such that real-time diagnoses of growing cumulus clouds can be used to linearly extrapolate trends up to 2-h time periods. The OT method improves cloud tracking over the single-pixel approach of Mecikalski and Bedka (2006) yet preserves the use of cumulus-cloud-specific identification via the CCM and the utility of MAMVs to look for object overlap between successive geostationary satellite images.

For the skill assessments, 9943 CI nowcasts and 804 CI events were analyzed. The best results occurred in the central U.S./Great Plains domain, where the POD and FAR reached 85% and 55%, respectively, for tracked cloud objects, ignoring missed forecasts resulting from cirrus cloud contamination or an inability to track cloud objects. The FARs were attributed to difficulties inherent to the CI nowcasting problem (i.e., not all cumulus clouds maintain growth in a linear fashion) and to errors resulting from subgrid cloud growth, thin-cirrus contamination, and tracking. PODs were seen to decrease for CI events in Florida. Discussion is provided on why these statistical skill results vary as a function of geographical region, and include 1) variations in cloud development rates as a result of differences in instability (SBCAPE); 2) higher moisture contents in the more tropical environments, leading to warm-rain processes forming in new cumulus clouds at early stages, and therefore a shorter lead time for the detection of ≥35-dBZ rainfall intensities; and 3) tracking errors associated with slow or more random cumulus-cloud motions in advance of CI in coastal regions and in less dynamic synoptic environments. The best results (highest POD, lowest FAR, and longest lead times) were seen in the central United States/Great Plains, and the worst performance statistics were found in the more tropical location of Melbourne. Average nowcast lead times for the considered study regions were generally between 24 and 33 min, similar to findings from Mecikalski et al. (2008), yet individual outlier lead times ranged from 0 min to 2 h. Accuracies are greater than 90%, mainly because the algorithm correctly predicts non-CI events a significant portion of the time, whereas SATCASTv2 suffers overall

because CI events that occur under preexisting cirrus cloud decks cannot be detected (i.e., the class-3 results).

Overall, these skill score results likely demonstrate the predictability limits of a CI nowcast system that is based on linear extrapolation and constant thresholds, given the large subjectively analyzed dataset. Specifically, we come to this conclusion because not all growing cumulus clouds (despite reaching critical thresholds when observed with geostationary, 15–30-min-resolution IR-imagery interest fields) attain CI, for reasons related to the presence of capping inversions, short-lived updrafts, limited moisture, and/or strong wind shear (that weakens or destroys an updraft).

Improvements to the overall SATCASTv2 algorithm will come as the result of improvements to its integral components and input data. As evidenced from this study, two improvements that would prove very beneficial to the algorithm include a changeover to dynamic (nonglobal) interest-field thresholds to better fit regional conditions (such as in the tropical environments of coastal Florida) and a further refinement of the cloud OT method to reduce residual errors even more so than the recent tracking-method enhancement.

It is believed, however, that many of these errors will be greatly diminished with use of higher temporal-, spatial-, and spectral-resolution data from newer generations of geostationary satellite instruments: the GOES-R series of instruments. Decreased intervals (5 min; Schmit et al. 2005) between successive satellite images will lead to a greater accuracy in the derivation of MAMVs and better overlapping between the same cloud objects in the cloud OT method. Furthermore, the availability of more spectral channels (16 total; Schmit et al. 2005) will allow for the use of more CI interest fields, which can provide additional information about the cloud-top characteristics needed to diagnose the potential vertical growth of convective clouds toward CI.

Ongoing enhancements to the SATCASTv2 algorithm will include the implementation of nighttime and satellite rapid-scan data operations. Beyond that, promising research is being performed to help with the forecasting of CI beneath thin cirrus (a significant problem, as revealed in the class-3 statistics above) as well as with the reduction of false alarms. Statistical approaches that include nonsatellite datasets (e.g., numerical weather prediction models) as input are currently being tested to help to optimize the CI interest fields, some of which have already produced preliminary statistics with FARs below 30% and PODs above 80% (not shown in the study presented here). The goal of the authors is to continue building upon the current SATCASTv2 framework and to incrementally transfer many of these new research findings into the operational algorithm as soon as possible.

Acknowledgments. The research performed in this study was supported by the National Aeronautics and Space Administration Advance Satellite Aviation Products (ASAP) initiative for the 2010 program. We also acknowledge Lori Schultz for her contributions in identifying improvements for the SATCASTv2 algorithm, as well as for fruitful discussion. We also thank three anonymous reviewers for constructive criticism that has significantly increased the quality of this paper.

REFERENCES

Ackerman, S. A., 1996: Global satellite observations of negative brightness temperature differences between 11 and 6.7 μm. *J. Atmos. Sci.,* **53,** 2803–2812.

——, R. A. Frey, and W. L. Smith, 1992: Radiation budget studies using collocated observations from AVHRR, HIRS/2, and ERBE instruments. *J. Geophys. Res.,* **97,** 11 513–11 525.

Bachmann, S., and D. Zrnić, 2007: Spectral density of polarimetric variables separating biological scatterers in the VAD display. *J. Atmos. Oceanic Technol.,* **24,** 1186–1198.

Banacos, P. C., and D. M. Schultz, 2005: The use of moisture flux convergence in forecasting convective initiation: Historical and operational perspectives. *Wea. Forecasting,* **20,** 351–366.

Baum, B. A., P. F. Soulen, K. I. Strabala, M. D. King, S. A. Ackerman, W. P. Menzel, and P. Yang, 2000: Remote sensing of cloud properties using MODIS airborne simulator imagery during SUCCESS. 2. Cloud thermodynamic phase. *J. Geophys. Res.,* **105,** 11 781–11 792.

Bedka, K. M., and J. R. Mecikalski, 2005: Application of satellite winds to mesoscale phenomena and nowcasting. *J. Appl. Meteor.,* **44,** 1761–1772.

——, C. S. Velden, R. A. Petersen, W. F. Feltz, and J. R. Mecikalski, 2009: Comparisons of satellite-derived atmospheric motion vectors, rawinsondes, and NOAA Wind Profiler observations. *J. Appl. Meteor. Climatol.,* **48,** 1542–1561.

Berendes, T. A., J. R. Mecikalski, W. M. Mackenzie, K. M. Bedka, and U. S. Nair, 2008: Convective cloud identification and classification in daytime satellite imagery using standard deviation limited adaptive clustering. *J. Geophys. Res.,* **113,** D20207, doi:10.1029/2008JD010287.

Browning, K. A., and D. Atlas, 1965: Initiation of precipitation in vigorous convective clouds. *J. Atmos. Sci.,* **22,** 678–683.

Chang, F., and Z. Li, 2003: Detecting and evaluating the effect over overlaying thin cirrus cloud on MODIS retrieved water-cloud droplet effective radius. *Extended Abstracts, 13th ARM Science Team Meeting Proceedings,* Broomfield, CO, U.S. Dept. of Energy, 6 pp. [Available online at http://www.arm.gov/publications/proceedings/conf13/extended_abs/chang1-fl.pdf.]

Easterling, D. R., and P. J. Robinson, 1985: The diurnal variation of thunderstorm activity in the United States. *J. Climate Appl. Meteor.,* **24,** 1048–1058.

Engel, C., and E. Ebert, 2007: Performance of hourly operational consensus forecasts (OCFS) in the Australian region. *Wea. Forecasting,* **22,** 1345–1359.

Harris, R. J., J. R. Mecikalski, W. M. MacKenzie Jr., P. A. Durkee, and K. E. Nielsen, 2010: The definition of GOES infrared lightning initiation interest fields. *J. Appl. Meteor. Climatol.,* **49,** 2527–2543.

Huang, X., Y. Ma, and G. A. Mills, 2008: Verification of mesoscale NWP forecasts of abrupt wind changes. Centre for Australian Weather and Climate Research Tech. Rep. CTR008, 67 pp.

Li, X., C.-H. Sui, and K.-N. Lau, 2002: Precipitation efficiency in the tropical deep convective regime: A 2-D cloud resolving modeling study. *J. Meteor. Soc. Japan,* **80,** 205–212.

Marshall, J. S., and S. Radhakant, 1978: Radar precipitation maps as lightning indicators. *J. Appl. Meteor.,* **17,** 206–212.

Mecikalski, J. R., and K. M. Bedka, 2006: Forecasting convective initiation by monitoring the evolution of moving cumulus in daytime GOES imagery. *Mon. Wea. Rev.,* **134,** 49–78.

——, S. J. Paech, K. M. Bedka, and L. A. Litten, 2008: A statistical evaluation of GOES cloud-top properties for nowcasting convective initiation. *Mon. Wea. Rev.,* **136,** 4899–4914.

——, W. M. Mackenzie, M. Koenig, and S. Muller, 2010: Cloud-top properties of growing cumulus prior to convective initiation as measured by Meteosat Second Generation. Part I: Infrared fields. *J. Appl. Meteor. Climatol.,* **49,** 521–534.

Mueller, C., T. Saxen, R. Roberts, J. Wilson, T. Betancourt, S. Dettling, N. Oien, and J. Yee, 2003: NCAR Auto-Nowcast System. *Wea. Forecasting,* **18,** 545–561.

Murray, J. J., 2002: Aviation weather applications of Earth Science Enterprise data. *Earth Obs. Mag.,* **11** (8), 26–30.

Prata, A. J., 1989: Observations of volcanic ash clouds in the 10-12 μm window using AVHRR/2 data. *Int. J. Remote Sens.,* **10,** 751–761.

Roberts, R. D., and S. Rutledge, 2003: Nowcasting storm initiation and growth using *GOES-8* and WSR-88D data. *Wea. Forecasting,* **18,** 562–584.

——, and Coauthors, 2008: REFRACTT 2006. *Bull. Amer. Meteor. Soc.,* **89,** 1535–1548.

Saunders, R., 1986: An automated scheme for the removal of cloud contamination from AVHRR radiances over western Europe. *Int. J. Remote Sens.,* **7,** 867–886.

Schmetz, J., S. A. Tjemkes, M. Gube, and L. van de Berg, 1997: Monitoring deep convection and convective overshooting with METEOSAT. *Adv. Space Res.,* **19,** 433–441.

Schmit, T. J., M. M. Gunshor, W. P. Menzel, J. J. Gurka, J. Li, and A. S. Bachmeier, 2005: Introducing the next-generation advanced baseline imager on GOES-R. *Bull. Amer. Meteor. Soc.,* **86,** 1079–1096.

Sieglaff, J. M., L. M. Cronce, W. F. Feltz, K. M. Bedka, M. J. Pavolonis, and A. K. Heidinger, 2011: Nowcasting convective storm initiation using satellite-based box-averaged cloud-top cooling and cloud-type trends. *J. Appl. Meteor. Climatol.,* **50,** 110–126.

Strabala, K. I., S. A. Ackerman, and W. P. Menzel, 1994: Cloud properties inferred from 8–12 μm data. *J. Appl. Meteor.,* **33,** 212–229.

Trentmann, J., and Coauthors, 2009: Multi-model simulations of a convective situation in low-mountain terrain in central Europe. *Meteor. Atmos. Phys.,* **103,** 95–103.

Velden, C. S., C. M. Hayden, S. J. Nieman, W. P. Menzel, S. Wanzong, and J. S. Goerss, 1997: Upper-tropospheric winds derived from geostationary satellite water vapor observations. *Bull. Amer. Meteor. Soc.,* **78,** 173–195.

——, T. Olander, and S. Wanzong, 1998: The impact of multispectral *GOES-8* wind information on Atlantic tropical cyclone track forecasts in 1995. Part I: Dataset methodology, description, and case analysis. *Mon. Wea. Rev.,* **126,** 1202–1218.

Wakimoto, R. M., and J. K. Lew, 1993: Observations of a Florida waterspout during CaPE. *Wea. Forecasting,* **8,** 412–423.

Walker, J. R., and J. R. Mecikalski, 2011: Algorithm theoretical basis document (ATBD) for convective initiation. NOAA NESDIS Center for Satellite Applications and Research, 40 pp. [Available online at http://www.nsstc.uah.edu/SATCAST/docs/GOES-R%20AWG%20ATBD%20Aviation%20ConvectiveInitiation%20v2.0.pdf.]

Weckwerth, T. M., and C. B. Parson, 2006: A review of convective initiation and motivation for IHOP_2002. *Mon. Wea. Rev.,* **134,** 5–22.

Wilson, J. W., and W. E. Schreiber, 1986: Initiation of convective storms by radar–observed boundary-layer convergence lines. *Mon. Wea. Rev.,* **114,** 2516–2536.

——, and C. K. Mueller, 1993: Nowcasts of thunderstorm initiation and evolution. *Wea. Forecasting,* **8,** 113–131.

——, J. A. Moore, G. B. Foote, B. Martner, A. R. Rodi, T. Uttal, and J. M. Wilczak, 1988: Convective Initiation and Downburst Experiment (CINDE). *Bull. Amer. Meteor. Soc.,* **69,** 1328–1348.

——, G. B. Foote, N. A. Crook, J. C. Fankhauser, C. G. Wade, J. D. Tuttle, C. K. Mueller, and S. K. Kruger, 1992: The role of boundary–layer convergence zones and horizontal rolls in the initiation of thunderstorms: A case study. *Mon. Wea. Rev.,* **120,** 1785–1815.

Zinner, T., H. Mannstein, and A. Tafferner, 2008: Cb-TRAM: Tracking and monitoring severe convection from onset over rapid development to mature phase using multi-channel *Meteosat-8* SEVIRI data. *Meteor. Atmos. Phys.,* **101,** 191–210.